nature communications

Article

https://doi.org/10.1038/s41467-025-63853-w

Cocrystal effect-driven ultrafast phase-transition ionogel for dynamically switchable adhesion interfaces

Received: 22 April 2025

Accepted: 27 August 2025

Published online: 02 October 2025

Check for updates

Yan Zheng[1], Zhikai Dong[1], Shaochuan Luo[2,3,4], Qi jin[2,3,4], Songlin Tao[2,3,4], Yichen Ding[2,3,4], Tang Li[2,3,4], Xiaoliang Wang[2,3,4] ✉, Dongshan Zhou[2,3,4] ✉ & Shuangjun Chen[1] ✉

Smart adhesion materials are paramount to the construction of dynamic adhesion interfaces in domains such as flexible electronics, soft robotics, and precision manufacturing. Research focuses on resolving the inherent contradiction between material adhesion and switchability. Herein, we report a poly(ionic liquid)/ionic liquid cocrystal ionogel that combines the advantages of polymer and small-molecule phase transitions, enabling rapid and repeated switching between strong-weak adhesion states while simultaneously converting adhesion changes into electrical signal feedback to the external environment. The study shows that the long alkyl chains in the two components form a cocrystal structure, with the crystallization-melting temperature precisely controlled by the alkyl chain length (−10 to 60 °C). The ultrafast phase transition ($t_{1/2}$ < 1 ms) of the ionogels leads to significant changes in the viscoelastic/electrical behavior, thereby inducing switching in adhesion (peel strength >1000 N/m, switching ratio >120) and electrical properties (switching ratio: 10^2–10^3). Based on the adhesion-electrical coupling effect, we design a dual-mode smart capture patch with dynamically feedback-regulated adhesion to enable objects' free pickup and release. This work provides a pathway for designing smart adhesive materials for dynamic adhesion interfaces.

Dynamically switchable adhesive interfaces are ubiquitous in natural systems and industrial applications, playing critical roles across multiple domains. A prime biological example is the gecko's ability to navigate vertical surfaces and inverted ceilings with effortless adhesion switching, enabling predator evasion and prey capture[1]. In advanced manufacturing sectors, including semiconductor fabrication, precision electronics, and optical engineering, such interfaces are indispensable for temporary component fixation and surface protection[2]. The rapid development of flexible electronics, advanced medicine, and intelligent robotics has driven increasingly complex and diverse requirements for switchable adhesion interfaces[3–5]. These intelligent dynamic interfaces aim to achieve: (i) Rapid, reversible transitions between strong and weak adhesion states under targeted stimuli, and (ii) Real-time adhesion-state feedback through detectable signals (e.g., electrical, optical) to enable precision manipulation, a capability attracting growing research attention[6,7]. Conventional adhesive materials, however, remain fundamentally constrained by trade-offs between adhesion strength and switching performance, while lacking feedback capabilities. These limitations hinder their ability to meet the

[1]Department of Polymer Science and Engineering, College of Materials Science and Engineering, Nanjing Tech University, Nanjing, Jiangsu, China. [2]Department of Polymer Science and Engineering, School of Chemistry and Chemical Engineering, Nanjing University, Nanjing, Jiangsu, China. [3]State Key Laboratory of Coordination Chemistry, Nanjing University, Nanjing, Jiangsu, China. [4]Key Laboratory of High-Performance Polymer Material and Technology, Nanjing University, Nanjing, Jiangsu, China. ✉e-mail: wangxiaoliang@nju.edu.cn; dzhou@nju.edu.cn; chenshuangjun@njtech.edu.cn

multifaceted requirements of next-generation smart adhesion systems for emerging applications.

Significant advances have recently been achieved in strong adhesive materials through strategies including dynamic chemical bonding, catechol modification, filler composites, crystalline domains, and microphase separation[8–15]. These strategies all emphasize the critical role of interfacial interactions and the material's internal energy dissipation capacity in adhesion strength. For manipulating the adhesion strength, the use of external stimuli (thermal, light, electromagnetic fields, humidity, chemical stimuli, etc.) to trigger polymer viscoelastic changes is the basic idea, as the energy dissipation capacity is a dynamic manifestation of polymer viscoelasticity[16–23]. Among existing methods, adhesion switching induced by the crystallization-melting transition of crystals has attracted widespread attention due to its substantial modulus variation and convenient operating conditions. Unfortunately, the adhesion switching performance of such materials (switching ratio <10, switching time >1 min) still falls short of meeting practical demands for high switching ratios and rapid responses, such as in robotic grippers and climbing robots[24,25]. Addressing these limitations necessitates consideration of both polymer and small-molecule crystallization processes. In general, the transition temperature of crystalline polymers can be successively adjusted, meeting the requirements for trigger temperatures in different scenarios[26–28]. Yet the incomplete crystallization of polymers results in a restricted viscoelastic tuning window and a wide temperature region for the phase transition process. Meanwhile, the slow crystallization speed severely limits the adhesion switching speed. In contrast, small molecule materials theoretically achieve complete crystallization, exhibit significant solid-liquid transitions within a narrow temperature range, and possess high crystallization speeds. However, their phase transitions are vulnerable to polymer matrix interference and lack continuous temperature tunability[29–31]. Moreover, systems requiring high small-molecule fractions (>50%) for substantial switching ratios present leakage risks.

A cocrystal constitutes a distinct single-crystalline phase solid material formed through non-covalent interactions between two or more molecular/ionic components at specific stoichiometric ratios. Its physical properties, including crystal structure, melting point, and solubility, differ markedly from those of the constituent precursors. This characteristic has been widely applied in fields such as pharmaceutical formulations, functional materials, and chemical separation[32–36]. Although cocrystals are mostly found in small molecule systems, polymer/small molecule cocrystals can form under specific conditions, e.g., polyacrylic acid long-chain alkyl ester/long-chain alkyl acid system[37]. Owing to the inherent high molecular weight and polydispersity of polymers, polymer-small molecule cocrystals exhibit unusually wide compositional tolerance windows. If polymer/small molecule cocrystal systems can combine the advantages of both crystallization behaviors, it is expected to provide a new option for switchable adhesion materials.

Building upon these premises, this work reports the first example of a poly(ionic liquid)/ionic liquid (PIL/IL) cocrystal material consisting of imidazole-based PIL and IL modified by long-chain alkyl groups. Due to structural similarity, small-molecule IL can be inserted into the alkyl side-chain lattice of PIL to form cocrystals. This material inherits the advantages of PIL and IL in crystallization, adhesion, and electrical conductivity, and thus exhibits a wide range of continuously tunable crystallization-melting transition temperatures, a narrow transition temperature region, excellent adhesion strength, high adhesion/electrical switching ability, and a high switching speed. We systematically investigate phase-transition temperature modulation, adhesive performance, and electrical characteristics while elucidating the adhesion-switching mechanism and crystallization kinetics. Furthermore, we engineer an electrically controlled adhesion-feedback bifunctional smart capture patch, validating the cocrystal material's dual-functional capabilities for switchable adhesion and smart feedback applications.

Results

Significantly differing from simple polymer crystallization or small-molecule crystallization, polymer/small-molecule cocrystals involve both components entering the lattice, as shown in Fig. 1a. Consequently, it can be expected that the cocrystal will have some of the characteristics of both polymer and small molecule crystallization. For instance, cocrystal materials display more pronounced viscoelastic changes during phase transitions compared to crystalline polymers. This occurs because small molecules enhance material crystallinity in the solid state but act as plasticizers in the molten state. Furthermore, the phase transition temperature can be easily and continuously regulated by adjusting the polymer molecular weight or side chain structure and the polymer/small molecule ratio. Small molecules with strong crystallization tendencies also promote higher crystal perfection within the cocrystal, leading to a narrower phase transition temperature range. Highly mobile small molecules additionally facilitate the regulation of crystallization kinetics.

To validate this concept, we designed two imidazolium-based ionic liquids with long alkyl chains: VC_xImTFSI and MC_xImTFSI (Fig. S1). The only difference between them is that VC_xImTFSI has a polymerizable double bond attached to the N atom whereas MC_xImTFSI is attached to a nonpolymerizable methyl group (where $x = 14, 16, 18, 20, 22$, denoting the alkyl chain carbon count). Due to the symmetrical and regular structure of the long-chain alkyl chains, they have good crystallinity and the chain length controls the crystals's phase transition temperature. Upon UV curing, VC_xImTFSI polymerizes into a PIL_x with crystallizable side chains, while MC_xImTFSI is uniformly distributed in the polymer network. Owing to their high mobility and structural similarity, the side-chain alkyl groups of PIL and the long-chain alkyl groups of IL will form a cocrystal at the right temperature (Fig. 1b).

Above the cocrystal melting point ($T > T_m$), the IL is liberated from the lattice and plasticizes the PIL network. The PIL/IL ratio governs the gel's viscoelasticity. Under slight pressure, the cocrystal gel flows and thus comes into close contact with the target object's surface. Diverse interfacial interactions, including hydrogen bonding and electrostatic forces, combined with the gel's energy dissipation capacity, provide robust adhesion strength, consistent with reports on highly adhesive ionogels[38–41]. When the cocrystal gel is required to detach from the surface of an object, adhesion switching can be achieved by cooling the gel below the crystallization temperature, bringing it into the crystalline state ($T < T_c$). In this state, molecular chain mobility is constrained by extensive crystalline regions, rendering the gel hard and brittle. The adhesion interface is prone to brittle damage, which greatly weakens the adhesion strength. This has been well demonstrated by other researchers and our previous work[27,42]. It is worth mentioning that since the conductive IL is a component of the cocrystal, its mobility is strongly constrained by the crystalline region. Thus, the cocrystal gel exhibits not only switchable adhesion but also switchable conductivity between its crystalline and amorphous states. This is very beneficial for evaluating the adhesion state of the material by monitoring the electrical properties. Leveraging this distinctive cocrystal behavior, our cocrystal gel has strong adhesion, high adhesion/electrical switching ratio, widely adjustable phase transition temperature, and high switching speed (Fig. 1c). This has never been reported in other work.

Past studies have shown that the T_m of IL is closely related to molecular size, symmetry, and charge distribution. As shown in Figs. 2a, b, and S2, lengthening the alkyl chains of IL increases intermolecular van der Waals forces, thereby elevating their T_m. When VC_xImTFSI was polymerized to form PIL_x, the resulting phase transition behavior exhibited characteristics typical of side-chain crystalline polymers (Fig. 2c). Specifically, longer alkyl side chains enhanced both

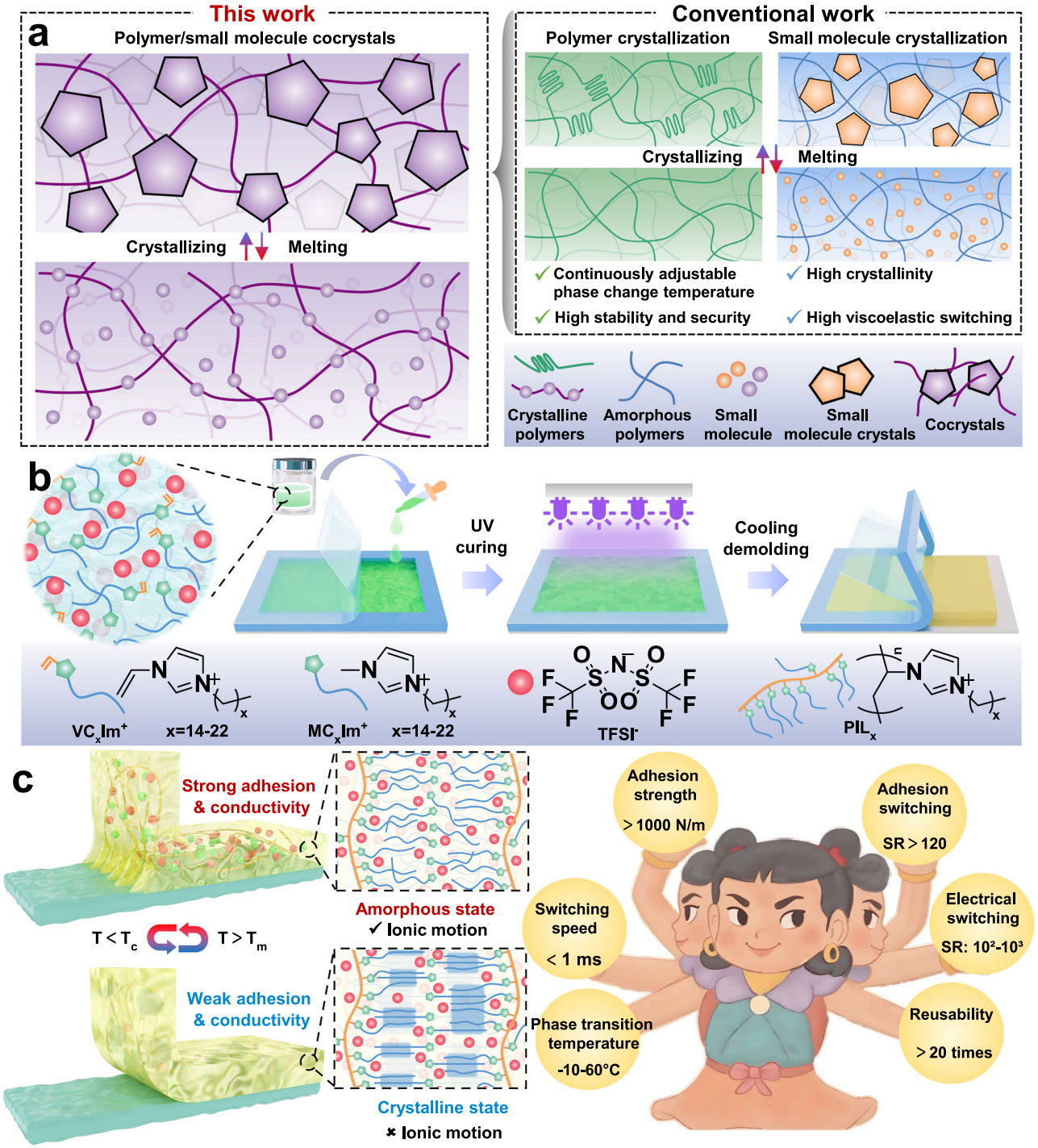

Fig. 1 | Design, preparation, and working principle of cocrystal ionogels. a Phase transition processes in polymer-small molecule cocrystals, polymer crystals, and small molecule crystals. **b** Structural design and preparation process of cocrystal ionogels. **c** Switching properties of cocrystal ionogels due to phase transitions.

crystallization capability and phase transition temperatures. For PIL_{14}, its alkyl side chains are too short resulting in almost no crystallization, while PIL_{16} exhibited only weak crystallization. As the side chains exceeded 18 carbons, PIL_x begins to show obvious crystallization, especially PIL_{20} and PIL_{22}. Corresponding to the DSC results, PIL_{14} remained transparent, PIL_{18} appeared translucent, and PIL_{22} became fully opaque (Fig. 2d). The XRD results show that PIL exhibits a diffraction peak at 22°, representing the crystallization of side-chain alkyls (Fig. 2e). In fact, the crystallization behavior of PIL_x is similar to the findings of Jordan et al. on the crystallization behavior of poly(n-alkyl acrylate) [43]. They found that the side chain exhibited crystalline behavior only if the number of side chain alkyl carbon atoms was greater than 12. In our system, the presence of a rigid imidazole ring and $TFSI^-$ resulted in a partial loss of PIL crystallization ability.

The situation changed significantly when small molecules of IL_x were added to PIL_x. The reduced transparency of PIL_{18}/IL_{18}-30% suggested enhanced crystallinity (Fig. 2f). Based on PIL_{18}, we investigated the phase transition behavior of PIL_{18}/IL_{18} cocrystal gels with different IL_{18} contents, as shown in Fig. 2g. The phase transition enthalpy of the gel increased significantly with the increase of IL_{18} percentage, while the phase transition temperature increased slightly (Fig. S3). What is more interesting is that the temperature range of the phase transition

https://doi.org/10.1038/s41467-025-63853-w

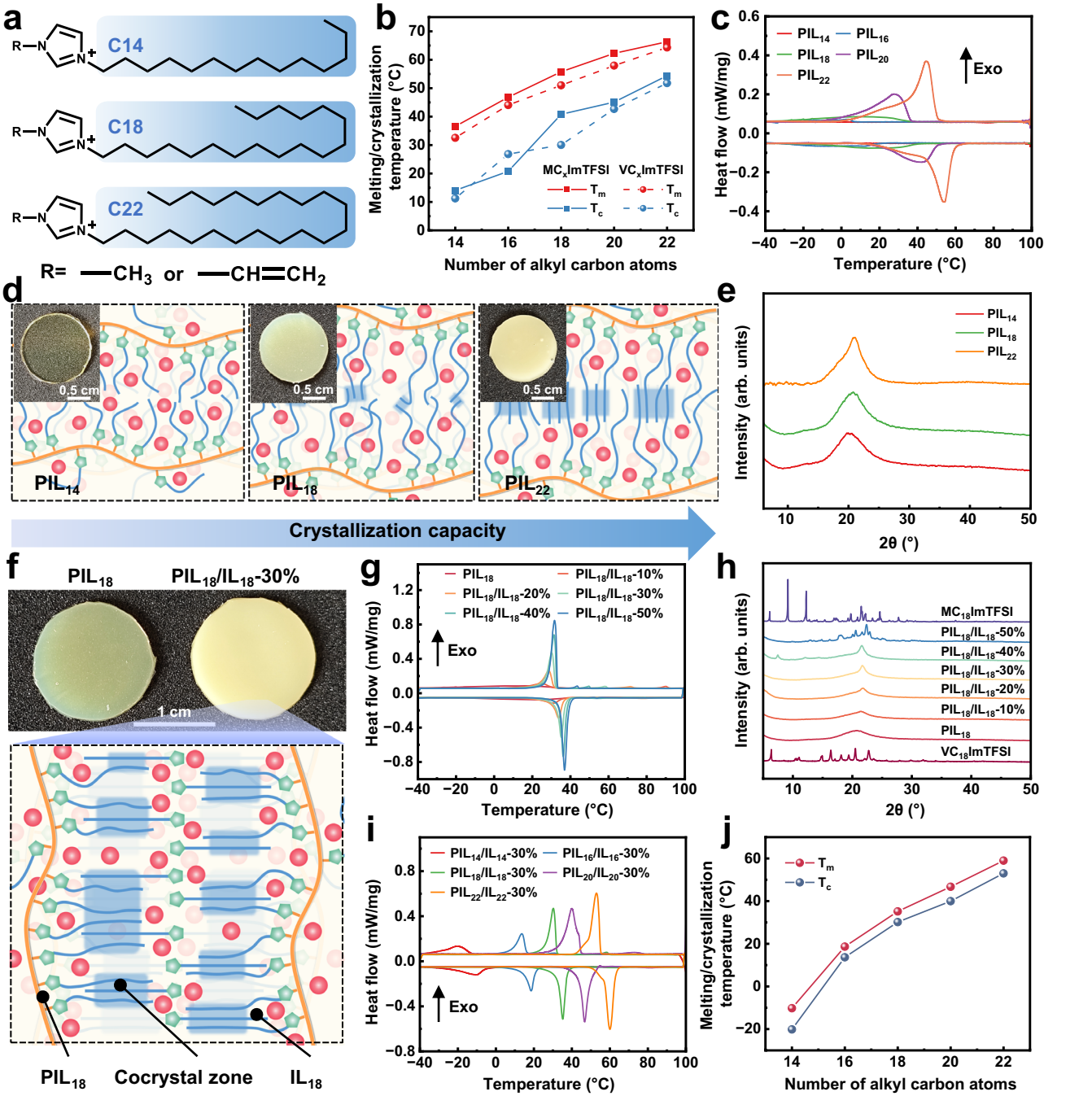

Fig. 2 | Phase transition behavior of cocrystal ionogels and its regulation. **a** Chemical structure of an imidazole cation with a long-chain alkyl group. **b** Relationship between alkyl group length and IL melting/crystallization temperature. **c** Effect of alkyl length on the melting/crystallization behavior of PIL_x measured by differential scanning calorimetry (DSC), and **d** the corresponding model diagram. **e** X-ray diffraction (XRD) pattern of PIL_x, tested at an ambient temperature of 25 °C. **f** Physical and model diagrams of PIL_{18}/IL_{18} cocrystal gels. **g** Melting/crystallization behavior of PIL_{18}/IL_{18} cocrystal gels at different IL contents and the corresponding (**h**) XRD patterns. **i** Melting/crystallization behavior of PIL_x/IL_x cocrystal gels at different alkyl lengths and the corresponding (**j**) phase transition temperatures, where the IL_x content was fixed at 30%.

process is narrowing accordingly and the supercooling effect is weakening (~5 °C). For example, the T_m and T_c of PIL_{18}/IL_{18}-20% were 33.7 and 28.8 °C, respectively. This result significantly differs from PIL and IL's respective phase transition behaviors. The DSC results indicate that the small molecules participate in the side-chain crystallization of PIL, leading to increased crystallinity and more perfect crystalline regions. The XRD and wide-angle X-ray scattering results of the cocrystal gel also support this view (Figs. 2h, S4). In samples with low IL_{18} content (content ≤ 40%), the crystallization peaks of IL_{18} itself disappear, while the signal peak at 22°, representing alkyl crystallization, shows an enhancement with the assistance of IL. Of course, excessive IL_{18} content in the PIL_{18} network not only participates in the cocrystal process but also aggregates and crystallizes on its own. For example, PIL_{18}/IL_{18}-50% exhibits diffraction peaks of pure IL_{18}, although lattice distortion causes a shift in the peak positions. Previous studies have found that long-chain imidazolium-based PIL and IL spontaneously form nanoscale layered structures under the influence of internal Coulombic or van der Waals forces[44–46]. These structures are

https://doi.org/10.1038/s41467-025-63853-w

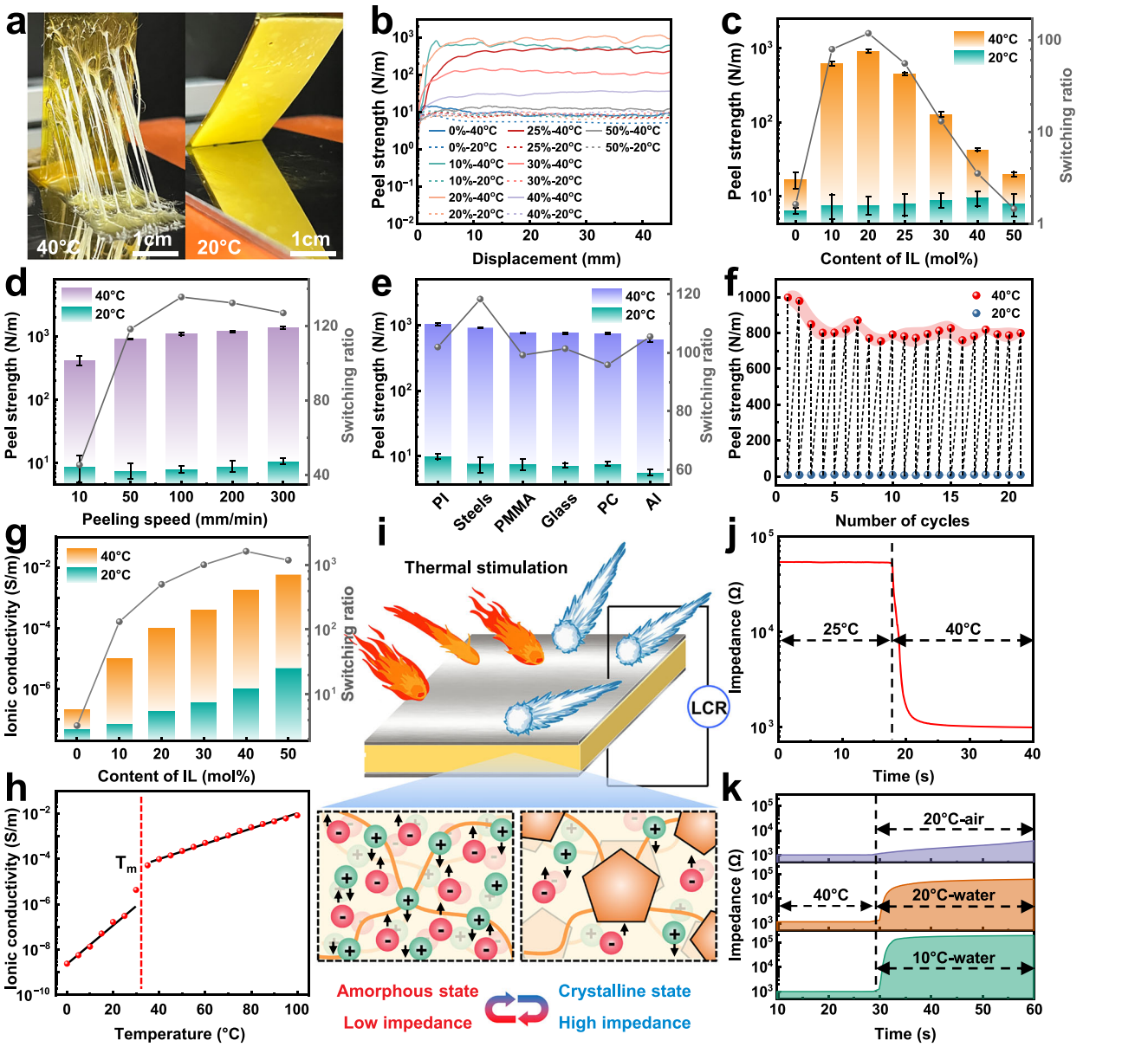

Fig. 3 | Adhesion and electrical properties regulation of cocrystal ionogels. **a** 90° peel images of sample PIL_{18}/IL_{18}-20% at 40 °C and 20 °C. Unless otherwise specified, the adhesion substrate used in experiments was stainless steel, and the peel speed was 50 mm/min. **b** Displacement-peeling strength curves and **c** plateau peeling strength of cocrystal gel with different IL contents at 40 °C and 20 °C. Effects of (**d**) peeling speed and **e** substrate on the peeling strength of cocrystal gel, with IL content fixed at 20%. **f** Reusability of cocrystal gel. **g** Ionic conductivity of cocrystal gel with different IL contents at 40 °C and 20 °C. **h** Relationship between ionic conductivity and temperature of cocrystal gel, with IL content fixed at 20%. **i** Schematic diagram of the cocrystal effect restricting ion movement. Impedance response of PIL_{18}/IL_{18}-20% cocrystal gel during the **j** heating-melting process and **k** cooling-crystallization process, tested at a frequency of 1 kHz. The electrodes used for the test were 15 μm-thick aluminum foil with dimensions of 2 × 2 cm. Data (**c**–**f**) are presented as the mean values ± SD, $n = 3$ independent samples. Source data are provided as a source data file.

very similar to those described in Fig. 2f, indirectly supporting our theory. Figure 2i shows that the cocrystal effect applies to all PIL_x/IL_x systems. Even PIL_{14}, which has the weakest crystallization ability, exhibits significant phase transitions with the help of IL_{14}. Furthermore, experiments demonstrate that by copolymerizing two $VC_xImTFSI$ with different alkyl chain lengths, the phase transition temperature of the gel can be effectively adjusted (Fig. S5). Ultimately, the phase transition temperature (T_m) of the PIL_x/IL_x series can be continuously tuned within the range of −10 to 60 °C (Fig. 2j).

Figure 3a illustrates representative peeling behaviors of cocrystal gels in amorphous and crystalline states. The gel exhibits cohesive failure at 40 °C but interfacial failure at 20 °C (40 °C > T_m, 20 °C < T_c). This demonstrates that phase state fundamentally governs adhesive properties, with IL content critically influencing both phase transition and viscoelasticity. Taking PIL_{18} as an example, we investigated the adhesive properties of PIL_{18}/IL_{18} cocrystal gels with different IL_{18} contents (Fig. 3b, c). The data show that the weakly crystalline pure PIL_{18} exhibits almost no adhesion at 40 °C and 20 °C (10.3 N/m at 40 °C), similar to most rigid PIL. With the incorporation of IL_{18}, the chain segment motility of PIL in the amorphous state is activated by the plasticizing effect of liquid small molecules, reducing elasticity but gradually revealing viscosity. The cocrystal gel flows under pressure within a short time and wets the substrate surface. The intermolecular interactions between the gel and the substrate (hydrogen bonding and

electrostatics) coupled with the gel's energy dissipation capacity contribute significantly to the adhesive strength[47]. At 20% IL_{18} loading, the gel achieves an optimal balance between elasticity and viscosity, resulting in a peeling strength of 906.7 N/m. Similarly, increasing the gel thickness to enlarge the energy dissipation zone also increases peeling strength (Fig. S6). Once the gel's viscoelasticity reaches an optimal balance, excessive IL will damage the gel's cohesive strength, leading to a decrease in peeling strength. However, when the gel is cooled to a rigid crystalline state, cocrystal gels with all ratios almost completely lose adhesion (<10 N/m). This results in an adhesion switching ratio ($SR = P_{adhesion}/P_{deadhesion}$) of up to 118.3.

In real life, adhesive interfaces are subjected to forces at different frequencies. Figure 3d shows peeling strength in the amorphous state increased substantially with peel speed, while remaining minimal and rate-independent in the crystalline state. For example, at 300 mm/min, the peeling strength of the gel at 40 °C and 20 °C is 1354 and 10.7 N/m, respectively, with a switching ratio as high as 127. This rate-dependence arises from enhanced viscoelastic dissipation within the polymer network under rapid deformation. Furthermore, we examined the adhesion of the cocrystal gel on different substrates to verify its broad applicability. Figure 2e shows that our cocrystal gel exhibits good adhesion and switching performance on various commonly used metals, inorganic materials, and plastics. In special cases, such as climbing robots or gripper devices, adhesive interfaces need to undergo repeated opening and closing. This requires repeatable switching of the adhesive material. Figure 3f shows that the cocrystal gel essentially maintained high adhesive strength and switching ability over 20 repeated cycles. The slight attenuation of the adhesion can be attributed to the contamination of the adhesion interface by trace dust and impurities on the substrate. The good environmental stability of cocrystal gels can be demonstrated by observing the effects of water soaking and high-temperature treatment on adhesion (Fig. S7).

As established, the conductive IL participates in the cocrystal lattice, where crystalline domains restrict IL mobility. This confinement results in markedly distinct electrical properties between amorphous and crystalline states (Fig. 3i). As expected, Fig. 3g shows that adding IL enables the gel to exhibit significant conductivity switching at 40 °C and 20 °C, and this effect is enhanced with increasing IL content. For the gel with 10% IL content, the SR is 132, while for the gel with 50% IL content, the SR reaches 1180. In comparison, the SR of pure PIL_{18} is only 3.28. To further confirm that this abrupt change in conductivity originates from the phase transition, we tested the ionic conductivity of the cocrystal gel with 20% IL content within the temperature range of 0–100 °C, as shown in Fig. 3h. The data indicate that the ionic conductivity of the gel exhibits a sharp jump only at T_m, while changes in other temperature regions follow the general Arrhenius temperature dependence. This significant change in electrical performance within a specific narrow temperature range for the cocrystal gel can be utilized to design smart temperature-sensitive switches[48]. Since the switching of both electrical properties and adhesion originates from the phase transition of the cocrystal, the two are deeply coupled. It becomes possible to determine the adhesion state by monitoring the electrical properties. Figure 3j, k show the impedance changes of the cocrystal gel under temperature stimulation. By applying a temperature stimulus of 40 °C to the gel at room temperature (25 °C), the gel transitions to a low-impedance amorphous state in ~2–3 s. Conversely, when temperature stimuli of 25 and 10 °C (water cooling) are applied to an amorphous gel (40 °C), the gel also switches to a high impedance crystalline state in about 2–3 s. Interestingly, gels cooled in air exhibit relatively slow impedance changes, which apparently results from the high air heat transfer resistance. Therefore, the phase transition speed should theoretically be faster, as unavoidable heat transfer resistance exists in reality. These results demonstrate sufficiently rapid switching for applications demanding high switching speeds. Comparative analysis in Table S1 further highlights our cocrystal gel's advantages over existing switchable adhesives.

Since the switchable adhesion of cocrystal gels originates from drastic viscoelastic changes, their rheological properties during temperature change are critical (Figs. 4a, b, S8). From the temperature sweep rheological curves of cocrystal gels, the following observations can be made: (1) The temperature range of the crystallization-melting transitions of cocrystal gels with different IL contents are basically the same, which is consistent with the results of DSC. (2) The addition of IL significantly increased the modulus difference of the gels before and after the phase transition. Taking the cocrystal gel with 20% IL as an example, its G′ (2.76×10^7) at 20 °C is much higher than G″ (4.49×10^6), indicating that the gel is a high-modulus solid at this time. At 40 °C, the cocrystal gel's G′ (1.43×10^5) and G″ (1.10×10^5) are close, and the gel is in a high-energy dissipation state with a balance between viscosity and elasticity. Many recent reports on adhesive materials have demonstrated that energy dissipation capacity is the source of strong adhesion[9,49]. (3) In addition to the crystallization-melting phase transition, another transition occurs in the high-temperature region of the cocrystal gel, and the transition temperature is directly related to the IL content. Based on previous work on long-chain IL and the results of DSC and polarized optical microscopy (Figs. S9–S11), it can be demonstrated that this transition is the liquid-crystal phase-isotropic phase transition[46]. Indeed, we speculate that the local order of the liquid crystal phase acts as a weak physical interaction, maintaining the gel's strength and enabling it to exhibit a viscous-elastic equilibrium between T_m and the isotropic transition temperature (T_i). Once the temperature is above T_i, the local ordering of the liquid crystals is disrupted. At this point, G″ is greater than G′ ($\tan\delta > 1$) and the gel exhibits liquid properties. Since the liquid crystal phase originates from the localized ordering of the PIL side chains, the addition of small molecules will disrupt this ordering to a certain extent, causing the localized ordering to shift to complete disorder prematurely. Therefore, the T_i of cocrystal gels decreases with the increase of IL content. The appearance of the liquid crystal phase will provide broader possibilities for the processing and functionalization of cocrystal gels[50,51].

During debonding process, cooling below T_c transitions the cocrystal gel into a rigid crystalline state, inducing bulk and interfacial changes. On the one hand, the gel undergoes significant volume shrinkage during crystallization, which introduces defects at the adhesion interface (Fig. S12). On the other hand, the cocrystal effect leads to an increase in gel modulus and a decrease in fracture elongation (Fig. 4c). For example, the modulus and fracture elongation of PIL_{18} are 90.7 MPa and 35.4%, respectively, whereas the modulus and fracture elongation of PIL_{18}/IL_{18}-20% are 121.3 MPa and 2.5%, respectively. The brittle gel is unable to dissipate energy through deformation. Therefore, during peeling, the adhesive interface is prone to failure at defect sites, resulting in low adhesive strength. This has been demonstrated in our previous work[42]. In addition to the adhesion switching, the surface properties of the cocrystal gel also undergo a drastic change. As shown in Fig. 4d, the coefficients friction of the cocrystal gels are 0.14, 1.28, and 1.97 at 20, 33 (T_m), and 40 °C, respectively. In comparison, the dynamic friction coefficient of low-friction polyethylene is 0.1-0.3. i.e. the cocrystal gels exhibit a slip-adhesion switch[52,53]. Changes in the frictional properties of the gel surface largely reflect changes in viscoelasticity as well.

The adhesion and electrical switching properties of cocrystal gels fundamentally arise from their crystallization-melting phase transition. Consequently, the switching speed is governed by crystallization kinetics, as crystallization is generally much slower than melting. Our previous work[42] has shown that alkyl side chains with high freedom degrees and regularity have high crystallization rates, and conventional DSC is unable to capture the complete crystallization process. Therefore, we used fast DSC, which has a high temperature-scanning

https://doi.org/10.1038/s41467-025-63853-w

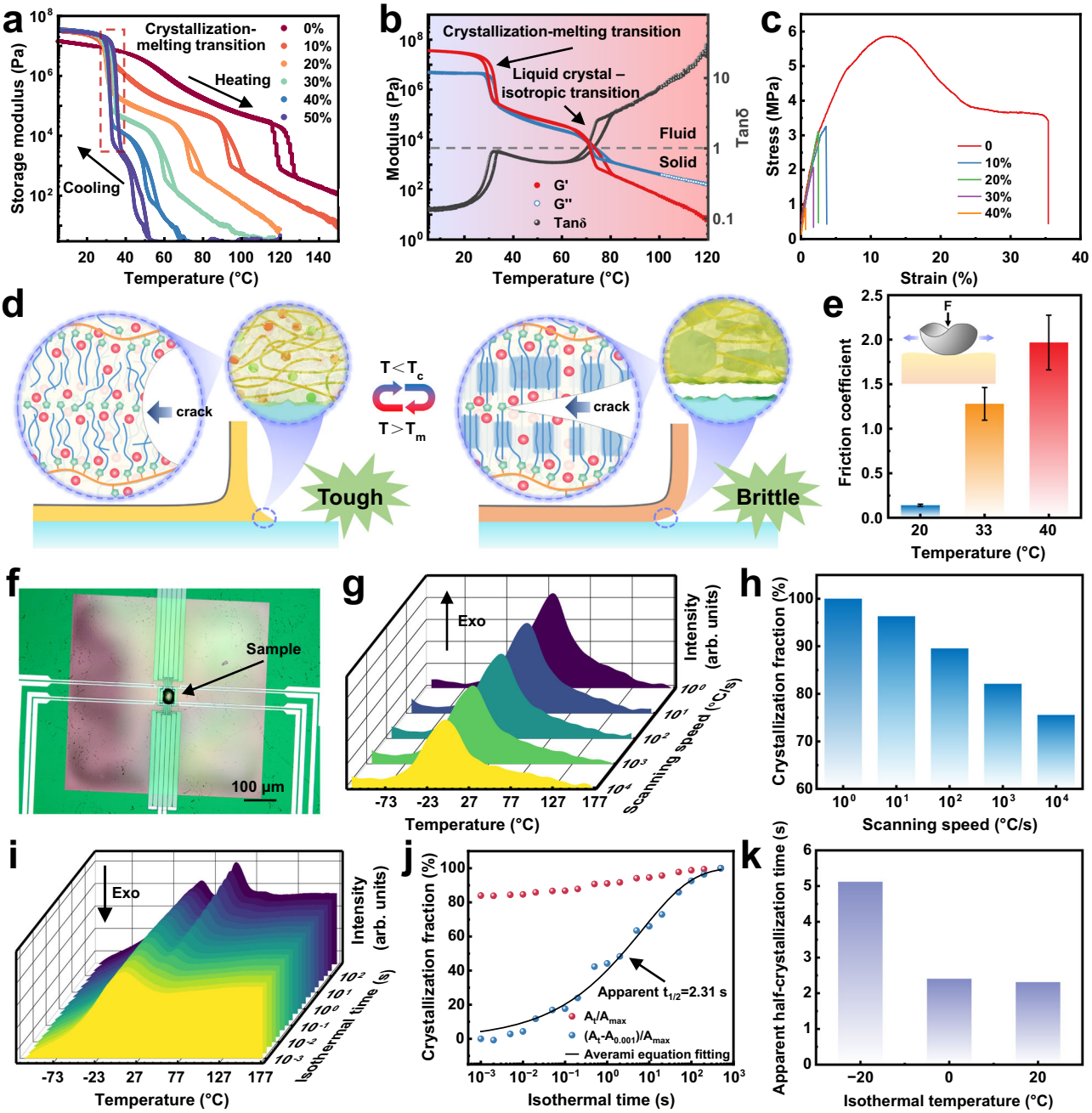

Fig. 4 | Adhesion switching mechanism and crystallization kinetics of cocrystal ionogels. a Storage modulus versus temperature for cocrystal gels with varying IL content. **b** Temperature-sweep rheological curves for gel with 20% IL content (0.1% strain, 1 Hz frequency, 2 °C/min ramp rate). **c** Tensile stress-strain curves of cocrystal gels at 20 °C. The cocrystal gel with 50% IL content is too brittle to be tested. **d** Schematic of peeling process for cocrystal gel in crystalline versus molten states, illustrating how the gel's microscopic state affects its macroscopic adhesion behavior. **e** Friction coefficient versus temperature for gel with 20% IL content. **f** Fast DSC specialized chip; arrow indicates trace cocrystal gel sample. **g** Crystallization exothermic curves and the corresponding **h** peak areas of cocrystal gels measured by fast DSC at different temperature scanning speeds, with 20% IL in the gel. **i** Isothermal time-melting heat flow signal curve, with an isothermal time range of 0.001-500 s and a cooling rate of 10,000 °C/s. **j** Relationship between crystallization fraction and isothermal time obtained from melt curves. The apparent half-crystallization time was obtained by fitting the isothermal time and apparent crystallization fraction through the Avrami equation. **k** Apparent half-crystallization time versus crystallization temperature, with a cooling rate of 10,000 °C/s. Data (**e**) are presented as the mean values ± SD, $n = 3$ independent samples. Source data are provided as a source data file.

rate, to study cocrystal gel crystallization kinetics. Figure 4f shows the fast DSC chip loaded with a trace amount of sample (μg level). Analysis of crystallization exotherms at different scanning rates provides an initial assessment of crystallization speed. Figure 4g shows that as the scanning speed increases, the subcooling effect causes the exothermic peak to shift to lower temperatures and the peak area decreases. Notably, crystallization persists even at 10,000 °C/s, indicating exceptionally rapid crystallization in the cocrystal gel. Taking the exothermic peak at 1 °C/s as a reference, the crystallization fraction can reach 75.5% at a scanning speed of 10,000 °C/s. The cocrystal gel transitions from an amorphous state at 40 °C to a crystalline state at 20 °C in just 2 ms. Further, we utilized isothermal crystallization experiments to evaluate the crystallization speed of the gel at different temperatures. Figure 4i, j show the melting curves and crystallization

fractions (A_t/A_{max}) of the gels during isothermal crystallization at 20 °C. The crystallization fraction of the gel reaches 84% when the isothermal time is 1 ms, indicating that the crystallization is almost completed within 1 ms. Since the crystallization speed exceeded the upper limit of the instrument's temperature change capability, it was not possible to obtain the precise half-crystallization time ($t_{1/2}$) at the target temperature, but a conservative estimate suggests that $t_{1/2} < 1$ ms. By subtracting the initial melting peak area ($(A_t\text{-}A_{0.001})/A_{max}$), it can be considered an apparent secondary crystallization process observed during 0.001-500 s. Fitting the results using the classic Avrami equation revealed an apparent $t_{1/2}$ of 2.31 s. As the isothermal temperature decreases, the mobility of polymers and small molecules is reduced, leading to a slower diffusion and orderly stacking toward the crystal nucleus. Therefore, the gel exhibits a longer $t_{1/2}$ at lower isothermal temperatures (Figs. 4k and S13). Although the cocrystal gel has a high crystallization speed, in practical situations, the gel's adhesion switching rate does not reach the millisecond level. This is due to the gel not instantly reaching the target crystallization temperature, and at this point, heat transfer resistance has become the rate-determining step.

To elucidate the cocrystal gel's rapid crystallization, we tested the crystallization rate of pure PIL_{18} at different temperatures. The data show that PIL_{18} has a high crystallization rate despite its low crystallinity (Figs. S14–S16). For example, the crystallization peak area of PIL_{18} at a scanning speed of 10,000 °C/s was 67.1% of that at 1 °C/s, and the apparent $t_{1/2}$ at 20 °C was 6.86 s. We speculate that the high crystallization speed of PIL is related to its molecular structure. The positively charged imidazole ring and its reverse charge ($TFSI^-$) are poorly compatible with the long-chain alkyl groups and tend to form a locally ordered liquid crystal state under the action of coulombic and van der Waals forces[54]. This pre-ordering characteristic of liquid crystal promotes nucleation and crystal growth, leading to high crystallization speeds. Indeed, the positive contribution of pre-ordering to the crystallization speed has been found in previous studies on the crystallization dynamics of conjugated polymers[55,56]. For cocrystal gels, it retains PIL's local ordering while incorporating highly mobile small molecules IL. The synergy of these factors enables the cocrystal gel's exceptional crystallization speed.

Leveraging the properties of cocrystal gels, we designed a dual-function smart capture patch. This device achieves voltage-controlled adhesion/detachment while monitoring the gel's adhesion state in real-time via impedance signals (Fig. 5a). One side of the smart capture patch integrates a Joule heating module, consisting of silver electrodes and a silver nanowires (AgNWs) coating. By adjusting the current of the AgNWs coating through the voltage applied between the silver electrodes, the Joule heat can be controlled. This enables the gel to achieve adhesion and deadhesion under voltage control. The opposite side of the smart capture patch is an impedance sensing module, composed of interdigitated electrodes and cocrystal gel. The impedance changes of the cocrystal gel during temperature variation and adhesion processes can be read in real-time through the interdigitated electrodes (Fig. 5b). Infrared imaging confirms uniform heating across the AgNW coating, with equilibrium temperature increasing proportionally to voltage (Fig. 5c). The device requires only a low driving voltage of 1.60 V to reach 102.7 °C, which covers the switching temperatures of a range of cocrystal gels and facilitates device miniaturization and operational safety. Given the strong temperature dependence of the gel's ionic conductivity, impedance signals directly correlate with temperature and thus adhesion state. Figures 5d and S17 show that during the on-off voltage process, the device's temperature (captured by an infrared camera) and impedance changes are completely synchronized, and even subtle temperature variations can be reflected in the impedance signal. After applying voltage, the device can reach equilibrium temperature in approximately 15 s. The cooling process, however, involves passive thermal dissipation, so the device takes a longer time to return to room temperature. Interestingly, from the temperature and impedance curves, fluctuations caused by phase transitions (T_m = 35 °C, T_c = 31 °C) can be observed, providing additional criteria for the adhesion state (Fig. S18). Figure 5e shows the equilibrium temperature and corresponding impedance at various operating voltages, indicating that the operating voltage must exceed 0.50 V to achieve an equilibrium temperature above T_m (the impedance at T_m being ~2×10^6 Ω). Within the voltage range of 0.25–1.60 V, the impedance changes by four orders of magnitude, demonstrating the high sensitivity of the feedback module. Furthermore, we tested the temperature and impedance changes of the device under repeated voltage switching. The results show consistent equilibrium temperature and impedance signals during the cycling process, demonstrating the reliability of the Joule heating and feedback modules (Fig. 5f).

Finally, we demonstrated its operation by using the smart capture patch to pick up a small glass bottle (Fig. 5g). In the single-voltage mode, a voltage of 1.15 V was input to the device, and the impedance rapidly decreased and then stabilized within 15 s (Fig. 5h). At this point, the device was in a strong adhesion state. When the device comes into contact with the bottle, the impedance signal rises instantaneously due to thermal transfer. As thermal equilibrium was gradually established, the impedance decreased and stabilized, indicating that the device was firmly bonded to the bottle. In this state, the target object could be manipulated and moved. When the object needs to be released, the adhesion strength can be reduced by turning off the voltage so that the adhesion interface automatically cools down to room temperature. A rise in impedance is observed at the moment the voltage is turned off, followed by fluctuations in impedance due to the crystallization phase change. Once crystallization was complete, the adhesion interface could be easily opened. At the moment the interface was opened, the impedance instantly increased and returned to its initial value. In fact, this process can be made even more smart. For example, to compensate for the temperature drop caused by contact with the object and to enable the gel to enter the strong adhesion state faster, the initial voltage can be adjusted to 1.30 V (Fig. 5i). After determining that the gel has entered the strong adhesion state through the impedance, the voltage can be lowered to 1.00 V. From the impedance signal, it can be determined that the gel's temperature remains stable under a voltage of 1.00 V. This prevents the temperature from continuing to rise while maintaining the gel's adhesion. The subsequent deadhesion process is the same as described above. Clearly, this approach of dynamically adjusting the voltage via impedance feedback demonstrates greater intelligence and is especially well-suited for scenarios with stringent requirements for both temperature and adhesion.

Discussion

This study designed a polymer/small molecule cocrystal gel and utilized its ultrafast melting-crystallization phase transition to achieve dynamic regulation of adhesion performance, successfully resolving the long-standing challenge of balancing high adhesion and switchability in conventional adhesives. Mechanistic investigations revealed that the crystalline domains formed by alkyl chain ordering in PIL and IL serve as the critical element enabling ultrafast reversible phase transitions. Precise control of phase transition temperature window (−10 to 60 °C) was achieved through alkyl chain length modulation. The synergistic interaction between PIL's pre-ordered structure and IL's high mobility endows the system with millisecond-scale crystallization capability, realizing synchronous switching of viscoelasticity and conductivity (peel strength >1000 N/m, adhesion switching ratio >120, conductivity switching ratio: 10^2-10^3). Leveraging these properties, an electrically controlled adhesive smart patch was developed. It can perform object grasping-releasing operations at a low voltage of 1.00 V and monitor the actions in real-time through impedance changes. While demonstrating significant progress, current limitations warrant attention. Such as thermal resistance effects compromise the

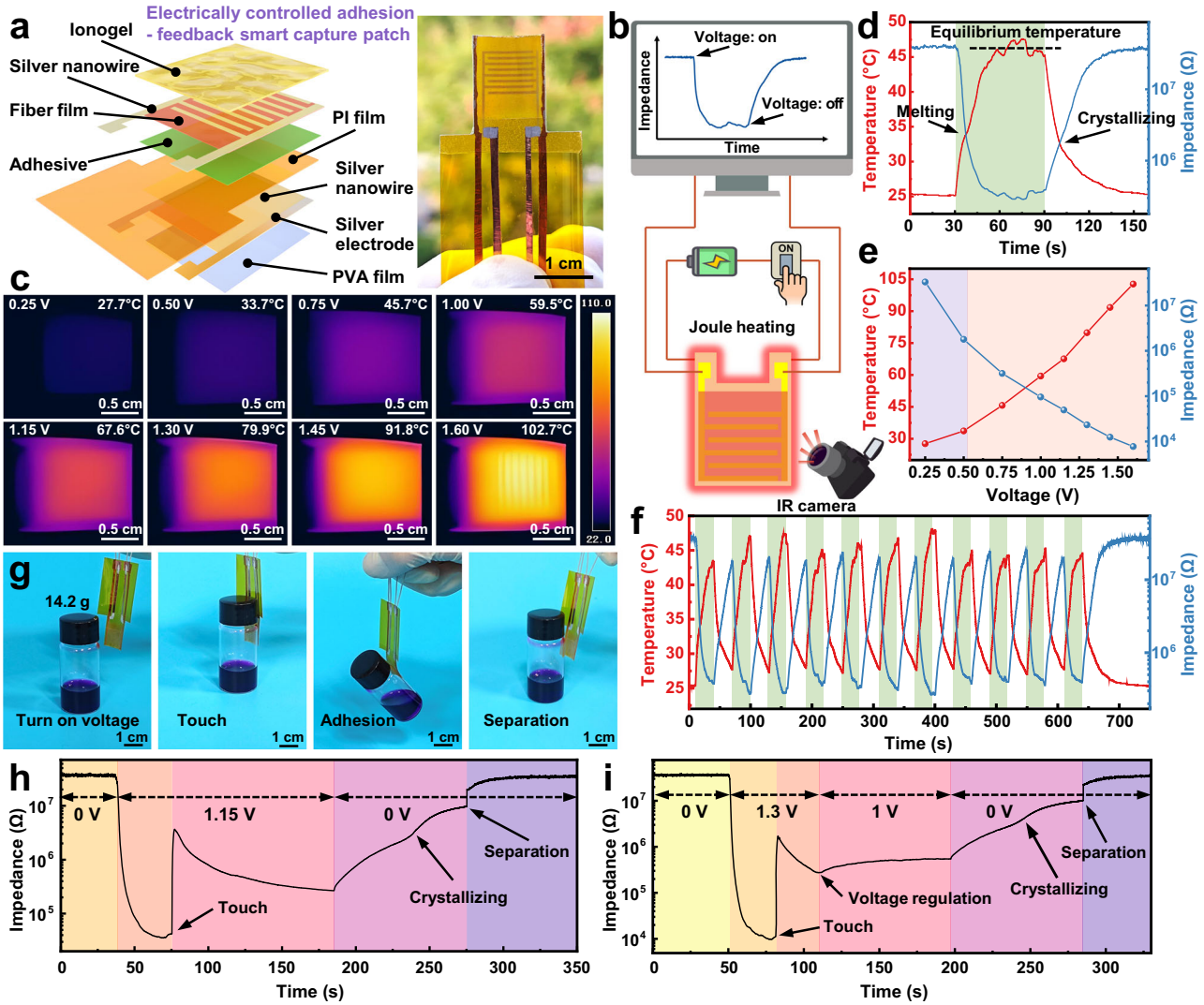

Fig. 5 | Application of cocrystal ionogels in smart adhesive interfaces. **a** Schematic and photograph of the electrically controlled adhesion-feedback dual-function smart capture patch. **b** Working mechanism of the smart patch. **c** Infrared thermal images of the patch under varying applied voltages. **d** Real-time temperature and impedance (1 kHz) of the smart capture patch at an operating voltage of 0.75 V. The green shaded area in the figure represents the time when the voltage is applied. **e** Relationship between operating voltage, equilibrium temperature, and impedance. **f** Transient temperature and impedance response under pulsed voltage stimulation (0.75 V, 20 s interval). **g** Sequential snapshots of the smart patch picking up and releasing a small glass bottle. Impedance signals generated by smart patches during the lifting/release of small glass bottles in modes (**h**) without and (**i**) with feedback adjustment.

theoretically predicted millisecond switching speed. Additionally, it is also worth considering how to introduce more energy dissipation mechanisms into the material without affecting the phase transition to further improve adhesion. This work establishes a novel paradigm for developing smart adhesive materials that combine high adhesion strength, rapid response, and signal feedback capabilities, showing substantial application potential in flexible electronics and soft robotics.

Methods

Materials

Lithium bis(trifluoromethanesulfonyl)imide (LiTFSI, 99%), 2,2-Dimethoxy-1,2-diphenylethanone (99%), N-methylimidazole (99%) and N-vinyl imidazole were purchased from Shanghai Aladdin Biochemical Technology Co., Ltd. 1-Bromotetradecane (98%), 1-Bromohexadecane (98%), 1-Bromooctadecane (98%), 1-Bromoicosane (97%), 1-Bromodocosane (98%) were purchased from Bailiwick Technology Ltd. Methanol and ethyl acetate were sourced from Shanghai Titan Technology Co. Silver nanowire dispersion (30 nm, 1%) was purchased from Zhejiang Kechuang Advanced Materials Technology Co.

Synthesis of ionic liquids $VC_xImTFSI$ and $MC_xImTFSI$

First, 0.105 mol of N-vinylimidazole, 0.1 mol of bromoalkane, and 30 ml of methanol were placed in a round-bottomed flask, while nitrogen was passed into the flask to exclude oxygen. The flask was placed in an oil bath at 70 °C, and the reaction was magnetically stirred for 24 h. The reaction product was dropped into 1 L of ethyl acetate, obtaining a white precipitate. The precipitate was collected by filtration, and the product was purified by recrystallization in ethyl acetate. The purified product (VC_xImBr) was dried under vacuum at 65 °C for 4 h to remove the solvent.

An appropriate amount of VC_xImBr was dissolved in deionized water at 70 °C to obtain a 0.25 mol/L solution. Then an aqueous solution of LiTFSI with the same concentration was added to it, where the molar ratio of VC_xImBr and LiTFSI was 1: 1.05. The product $VC_xImTFSI$ was in the lower layer of the mixed liquid. The $VC_xImTFSI$ was washed

with deionized water 3 times at 70 °C, and the washed product was dried under vacuum at 70 °C for 3 h.

MC_xImTFSI was prepared as above, except that N-methylimidazole was used instead of N-vinylimidazole.

Preparation of cocrystal ionogels

A quantitative amount of VC_xImTFSI, MC_xImTFSI, and photoinitiator (0.8% mol of the monomer) were melted and mixed at 60 °C, while the mixed ionic liquids were later added into molds (20 × 50 × 0.5 mm) prepared from glass sheets and silicone rubber. Note that the molds were placed on a heating plate at 60 °C so that the ionic liquids were kept in the liquid state. After the ionic liquid was added to the mold, a piece of transparent PET release film was placed over the upper surface of the mold. The mixed ionic liquids were then polymerized into a cocrystal gel under UV light irradiation (2.5 W, 20 min).

Preparation of dual-modal smart capture patch

The polyimide film (50 μm) was cut into the desired shape using a laser, and then the conductive silver paste was applied to the target area and cured at 70 °C. The silver nanowire dispersion (isopropanol, 0.5 mg/mL) was sprayed between the two electrodes to form an electrical pathway, and the resistance was controlled by the amount of spraying, which was about 12 Ω. The film was placed on a heating plate at 120 °C and heated for 20 min to sinter the silver nanowires. At this time, the resistance dropped to about 3.5 Ω. By spin-coating a layer of polyvinyl alcohol (5%, 2000 r/min, 60 s) on the surface of the silver nanowire conductive layer, the resistance can be effectively ensured to remain stable during use.

Fork finger electrodes were obtained by spraying silver nanowire dispersion on the surface of the capacitor tissue paper (10 μm) with the help of a mask. The capacitor tissue paper with fork-finger electrodes was adhered to the opposite side of the Joule heating device using ultra-thin double-sided adhesive tape (10 μm). Subsequently, the prepared cocrystal gel was transferred to the fork-finger electrode surface and the two were tightly bonded with the aid of heating.

Finally, copper wires were connected to the Joule heating electrode and the fork finger electrode with conductive silver paste, respectively, thus realizing electronically controlled heating and impedance signal acquisition.

Characterization

Thermal analysis characterization. A differential scanning calorimeter (Mettler Toledo DSC1) was used to analyze ionic liquids' and cocrystal gels' phase transition behavior. The temperature range of the test was −40 to 100 °C and the temperature scanning rate was 10 °C/min. To evaluate the crystallization speed of cocrystal gels, we used a fast DSC with an ultra-high temperature scan rate built by our group. During isothermal crystallization experiments, a small amount of sample was transferred to a fast DSC-specific chip with the aid of a microscope, and tested at a temperature scanning rate of 10,000 °C/s. The isothermal time was selected as 0.001–500 s.

Adhesive properties characterization. To test the adhesive properties of the materials, the light-cured cocrystal gel was transferred to the surface of polyimide tape used as a rigid backing. The sample size was 50 × 20 × 0.5 mm. The peel strength of the samples was obtained by performing 90° peeling on a universal material testing machine at a speed of 50 mm/min. Temperature control was achieved by adjusting the temperature of the heating plate under the substrate so that the peel strength could be measured at different temperatures. Each set of samples is tested 3–4 times to obtain the average peel strength.

Electrical performance characterization. The material was sandwiched between two stainless steel discs (diameter: 1.5 cm) and was heated at 60 °C before testing to improve the contact between the gel and the electrode. The electrodes were then connected to an electrochemical workstation (Shanghai Chenhua chi660e). The frequency-impedance characteristics of the samples were tested using the AC impedance mode (frequency 0.1–10^6 Hz, voltage 10 mV) and the ionic conductivity of the materials was calculated from the results. The determination of the ionic conductivity of the gel at different temperatures was achieved by placing the samples in a temperature-controlled oven. The impedance change of the cocrystal gel under temperature stimulation was detected by a digital bridge (Tonghui, TH2830). To reduce the resistance to heat transfer due to thickness, aluminum foil (15 μm) was used as the electrode in the experiments, and the thickness of the gel was controlled by spin-coating (1000 r/min, 60 s, 10 wt% ethyl acetate solution). The temperature stimulation source is a plastic sealing bag filled with constant temperature water. During the impedance test, the water bag can be quickly placed on the electrode surface to apply temperature stimulation.

Rheological characterization. The rheological behavior of the materials was investigated using a rotational rheometer (ARES-G2, TA instrument) operated in temperature ramp mode. The samples had a diameter of 25 mm and a thickness of 0.5 mm. During the testing process, a strain of 0.1% was applied, while the temperature was varied within the range of 10–70 °C at a temperature change rate of 2 °C/min. Additionally, the frequency was set to 1 Hz.

Performance characterization of smart capture patches. Place the capture patch on the support stand, leaving its peripheral area unconstrained. During testing, the ambient temperature was ~25 °C with a relative humidity of 45%. The Joule heating module and the impedance sensing module of the capture patches are respectively connected to the adjustable DC power supply (UNI-T, UTP1605S) and the LCR digital bridge. An infrared camera (FOTRIC, 226 s) was positioned above the device to capture the gel surface temperature, with an approximate distance of 25 cm between the camera and the device. Different voltages (0.25–1.60 V) are applied to the device through the DC power supply, and during this period, the temperature and impedance changes of the device are obtained by the infrared camera and the LCR digital bridge (with a frequency of 1 kHz).

Data availability

All data generated in this study are provided in the source data file. Any requests for additional information should be directed to the corresponding author and will be made available upon request. Source data are provided with this paper.

References

1. Autumn, K. et al. Evidence for van der Waals adhesion in gecko setae. *Proc. Natl. Acad. Sci. USA* **99**, 12252–12256 (2002).
2. Yan, Z. et al. Thermal release transfer printing for stretchable conformal bioelectronics. *Adv. Sci.* **4**, 1700251 (2017).
3. Jiang, Y. et al. Wireless, closed-loop, smart bandage with integrated sensors and stimulators for advanced wound care and accelerated healing. *Nat. Biotechnol.* **41**, 652–662 (2023).
4. Huang, J. et al. Electrically programmable adhesive hydrogels for climbing robots. *Sci. Robot* **6**, eabe1858 (2021).
5. Deng, J. et al. Electrical bioadhesive interface for bioelectronics. *Nat. Mater.* **20**, 229–236 (2021).
6. Lyu, Q., Li, M., Zhang, L. & Zhu, J. Structurally-colored adhesives for sensitive, high-resolution, and non-invasive adhesion self-monitoring. *Nat. Commun.* **15**, 8419 (2024).
7. Liu, Z. et al. Detectable adhesives: nondestructive detection of adhesion. *Adv. Funct. Mater.* **35**, 2413799 (2024).

8. Zhang, L. et al. Cellulose nanofiber-mediated manifold dynamic synergy enabling adhesive and photo-detachable hydrogel for self-powered E-skin. *Nat. Commun.* **15**, 3859 (2024).
9. Shi, Y., Wu, B., Sun, S. & Wu, P. Peeling–stiffening self-adhesive ionogel with superhigh interfacial toughness. *Adv. Mater.* **36**, 2310576 (2024).
10. Yao, L., Peng, X., Zhu, H., Zhang, Q. & Zhu, S. Robust transient semi-glue tape: ultrastrong adhesion empowered by water activation and self-locking. *Adv. Mater.* **36**, 2405511 (2024).
11. Zhou, T. et al. 3D printable high-performance conducting polymer hydrogel for all-hydrogel bioelectronic interfaces. *Nat. Mater.* **22**, 895–902 (2023).
12. Yang, S. et al. Stretchable surface electromyography electrode array patch for tendon location and muscle injury prevention. *Nat. Commun.* **14**, 6494 (2023).
13. Nogusa, T. et al. Tunable, reusable, and recyclable per-fluoropolyether periodic dynamic polymers with high underwater adhesion strength. *Matter* **6**, 2439–2453 (2023).
14. Liu, J. et al. Fatigue-resistant adhesion of hydrogels. *Nat. Commun.* **11**, 1071 (2020).
15. Liu, Y. et al. Highly Stretchable, Low-Hysteresis, and Adhesive TA@MXene-Composited Organohydrogels for Durable Wearable Sensors. *Adv. Funct. Mater.* **34**, 2315813 (2024).
16. Zhang, L. et al. Temperature-mediated phase separation enables strong yet reversible mechanical and adhesive hydrogels. *ACS nano* **17**, 13948–13960 (2023).
17. Wang, D. et al. Sensing-triggered stiffness-tunable smart adhesives. *Sci. Adv.* **9**, eadf4051 (2023).
18. Linghu, C. et al. Overcoming the adhesion paradox and switchability conflict on rough surfaces with shape-memory polymers. *Proc. Natl. Acad. Sci. USA* **120**, e2221049120 (2023).
19. Xiong, J. et al. Biocompatible tough ionogels with reversible supramolecular adhesion. *J. Am. Chem. Soc.* **146**, 13903–13913 (2024).
20. Huang, S.-C., Zhu, Y.-J., Huang, X.-Y., Xia, X.-X. & Qian, Z.-G. Programmable adhesion and morphing of protein hydrogels for underwater robots. *Nat. Commun.* **15**, 195 (2024).
21. Zhou, Y. et al. Reversible adhesives with controlled wrinkling patterns for programmable integration and discharging. *Sci. Adv.* **9**, eadf1043 (2023).
22. Zhao, J. et al. Magnetically actuated adhesives with switchable adhesion. *Adv. Funct. Mater.* **33**, 2305484 (2023).
23. Min, H. et al. Stiffness-tunable velvet worm-inspired soft adhesive robot. *Sci. Adv.* **10**, eadp8260 (2024).
24. Linghu, C. et al. Versatile adhesive skin enhances robotic interactions with the environment. *Sci. Adv.* **11**, eadt4765 (2025).
25. Liu, Z. & Yan, F. Switchable adhesion: on-demand bonding and debonding. *Adv. Sci.* **9**, 2200264 (2022).
26. Gao, M., Meng, Y., Shen, C. & Pei, Q. Stiffness variable polymers comprising phase-changing side-chains: material syntheses and application explorations. *Adv. Mater.* **34**, e2109798 (2022).
27. Gao, M. et al. Skin temperature-triggered, debonding-on-demand sticker for a self-powered mechanosensitive communication system. *Matter* **4**, 1962–1974 (2021).
28. Choi, G. et al. Motion-adaptive tessellated skin patches with switchable adhesion for wearable electronics. *Adv. Mater.* **37**, 2412271 (2024).
29. Liu, L. et al. A superstrong and reversible ionic crystal-based adhesive inspired by ice adhesion. *Angew. Chem. Int. Ed.* **60**, 8948–8959 (2021).
30. Jinkins, K. R. et al. Thermally switchable, crystallizable oil and silicone composite adhesives for skin-interfaced wearable devices. *Sci. Adv.* **8**, eabo0537 (2022).
31. Xi, S. et al. Reversible dendritic-crystal-reinforced polymer gel for bioinspired adaptable adhesive. *Adv. Mater.* **33**, 2103174 (2021).
32. Bolla, G., Sarma, B. & Nangia, A. K. Crystal engineering of pharmaceutical cocrystals in the discovery and development of improved drugs. *Chem. Rev.* **122**, 11514–11603 (2022).
33. Remenar, J. F. et al. Crystal engineering of novel cocrystals of a triazole drug with 1,4-dicarboxylic acids. *J. Am. Chem. Soc.* **125**, 8456–8457 (2003).
34. Wang, Y. et al. Cocrystals strategy towards materials for near-infrared photothermal conversion and imaging. *Angew. Chem. Int. Ed.* **57**, 3963–3967 (2018).
35. Liang, H. et al. Nanoencapsulation-induced second harmonic generation in pillararene-based host–guest complex cocrystals. *J. Am. Chem. Soc.* **145**, 2870–2876 (2023).
36. Chen, Y.-T. et al. Organic photothermal cocrystals: rational design, controlled synthesis, and advanced application. *Adv. Sci.* **10**, 2206830 (2023).
37. Inomata, K., Sakamaki, Y., Nose, T. & Sasaki, S. Solid-state structure of comb-like polymers having n-octadecyl side chains. 2. Crystalline-amorphous layered structure. *Polym. J.* **28**, 992–999 (1996).
38. Zhang, J. et al. Adhesive Zwitterionic poly(ionic liquid) with unprecedented organic solvent resistance. *Adv. Mater.* **36**, 2403039 (2024).
39. Ye, H., Wu, B., Sun, S. & Wu, P. Self-compliant ionic skin by leveraging hierarchical hydrogen bond association. *Nat. Commun.* **15**, 885 (2024).
40. Yu Z., Wu P. Water-resistant ionogel electrode with tailorable mechanical properties for aquatic ambulatory physiological signal monitoring. *Adva. Funct. Mater.* **31**, 2107226 (2021).
41. Wang, Y., Sun, S. & Wu, P. Adaptive Ionogel paint from room-temperature autonomous polymerization of α-thioctic acid for stretchable and healable electronics. *Adv. Funct. Mater.* **31**, 2107226 (2021).
42. Zheng, Y. et al. Skin temperature-triggered switchable adhesive coatings for wearing comfortable epidermal electronics. *Chem. Eng. J.* **488**, 150459 (2024).
43. Jordan, E. F., Feldeisen, D. W. & Wrigley, A. N. Side-chain crystallinity. I. Heats of fusion and melting transitions on selected homopolymers having long side chains. *J. Polym. Sci. Part A-1: Polym. Chem.* **9**, 1835–1851 (1976).
44. Zhang, Z.-K., Ding, S.-P., Xia, D.-L. & Xu, J.-T. Microphase separation with sub-3 nm microdomains in comb-like poly(n-alkyl acrylate) homopolymers facilitated by charged junction groups between the main chains and side chains. *ACS Macro Lett.* **12**, 1005–1011 (2023).
45. Pontoni, D., DiMichiel, M. & Deutsch, M. Temperature evolution of the bulk nano-structure in a homologous series of room temperature ionic liquids. *J. Mol. Liq.* **300**, 112280 (2020).
46. Goossens, K., Lava, K., Bielawski, C. W. & Binnemans, K. Ionic liquid crystals: versatile materials. *Chem. Rev.* **116**, 4643–4807 (2016).
47. Kim, J. et al. Snail-inspired dry adhesive with embedded microstructures for enhancement of energy dissipation. *Adv. Mater. Technol.* **4**, 1900316 (2019).
48. Zhou, Y. et al. Ultrasensitive ionic conductors with tunable resistance switching temperature enabled by phase transformation of polymer cocrystals. *Adv. Mater.* **36**, 2309568 (2024).
49. Yu, Z. & Wu, P. Underwater communication and optical camouflage ionogels. *Adv. Mater.* **33**, e2008479 (2021).
50. White, T. J. & Broer, D. J. Programmable and adaptive mechanics with liquid crystal polymer networks and elastomers. *Nat. Mater.* **14**, 1087–1098 (2015).
51. Feng, W., He, Q. & Zhang, L. Embedded physical intelligence in liquid crystalline polymer actuators and robots. *Adv. Mater.* **37**, 2312313 (2024).
52. Li, X., Wu, B., Sun, S. & Wu, P. Making sticky-slippery switchable fluorogels through self-adaptive bicontinuous phase separation. *Adv. Mater.* **36**, 2411273 (2024).

53. Wang, Q., Kong, X., Zhu, L., Zhe, J. & Fan, Y. A study on the tribological behavior of polyethylene. II. Effects of operating conditions on the friction behavior of polyethylene. *J. Appl. Polym. Sci.* **58**, 903–910 (1995).
54. Biswas, Y., Banerjee, P. & Mandal, T. K. From polymerizable ionic liquids to poly(ionic liquid)s: structure-dependent thermal, crystalline, conductivity, and solution thermoresponsive behaviors. *Macromolecules* **52**, 945–958 (2019).
55. Luo, S. et al. Observation of stepwise ultrafast crystallization kinetics of donor–acceptor conjugated polymers and correlation with field effect mobility. *Chem. Mater.* **33**, 1637–1647 (2021).
56. Luo, S. et al. Real-time correlation of crystallization and segmental order in conjugated polymers. *Mater. Horiz.* **11**, 196–206 (2024).

Acknowledgements

This work was financially supported by the National Natural Science Foundation of China (No. 22405121 to Y.Z., No. 52350346 to D.Z., and No. 22173046 to X.W.), the National Key R&D Program of China (No. 2020YFA0711504 to D.Z.), the Shenzhen Science and Technology Innovation Committee (JCYJ20200109150656717 to D.Z.), and the Jiangsu Funding Program for Excellent Postdoctoral Talent (to Y.Z.).

Author contributions

Y.Z. conceived the idea. Z.D., Q.J., S.T., Y.D., and T.L. conducted the experimental studies. S.L. provided theoretical and characterization assistance. Y.Z. wrote the paper. All authors read and revised the paper. X.W., D.Z., and S.C. provided guidance on the work.

Competing interests

The authors declare no competing interests.

Additional information

Supplementary information The online version contains supplementary material available at https://doi.org/10.1038/s41467-025-63853-w.

Correspondence and requests for materials should be addressed to Xiaoliang Wang, Dongshan Zhou or Shuangjun Chen.

Peer review information *Nature Communications* thanks the anonymous reviewers for their contribution to the peer review of this work. A peer review file is available.